Influence of High-Pressure Induced Lattice Dislocations and Distortions on Thermoelectric Performance of Pristine SnTe

Bowen Zheng(郑博文)[1†], Tao Chen(陈涛)[3,4†], Hairui Sun(孙海瑞)[1,2*], Manman Yang(杨曼曼)[5], Bingchao Yang(杨兵超)[1,2], Xin Chen(陈欣)[1,2], Yongsheng Zhang(张永胜)[1,2*], and Xiaobing Liu(刘晓兵)[1,2*]

[1]*Laboratory of High-Pressure Physics and Materials Science (HPPMS), School of Physics and Physical Engineering, Qufu Normal University, Qufu 273165, China*
[2]*Advanced Research Institute of Multidisciplinary Sciences, Qufu Normal University, Qufu 273165, China*
[3]*Key Lab of Photovoltaic and Energy Conservation Materials Institute of Solid State Physics, HFIPS, Chinese Academy of Sciences, Hefei 230031, China*
[4]*University of Science and Technology of China, Hefei 230026, China*
[5]*School of Electronic Engineering Huainan Normal University, Huainan 232038, China*

(Received 1 February 2024; accepted manuscript online 3 April 2024)

As a sister compound of PbTe, SnTe possesses the environmentally friendly elements. However, the pristine SnTe compounds suffer from the high carrier concentration, the large valence band offset between the L and Σ positions and high thermal conductivity. Using high-pressure and high-temperature technology, we synthesized the pristine SnTe samples at different pressures and systemically investigated their thermoelectric properties. High pressure induces rich microstructures, including the high-density dislocations and lattice distortions, which serve as the strong phonon scattering centers, thereby reducing the lattice thermal conductivity. For the electrical properties, pressure reduces the harmful high carrier concentration, due to the depression of Sn vacancies. Moreover, pressure induces the valence band convergence, reducing the energy separation between the L and Σ positions. The band convergence and suppressed carrier concentration increase the Seebeck coefficient. Thus, the power factors of pressure-sintered compounds do not deteriorate significantly under the condition of decreasing electrical conductivity. Ultimately, for a pristine SnTe compound synthesized at 5 GPa, a higher ZT value of 0.51 is achieved at 750 K, representing a 140% improvement compared to the value of 0.21 obtained using SPS. Therefore, the high-pressure and high-temperature technology is demonstrated as an effectively approach to optimize thermoelectric performance.

DOI: 10.1088/0256-307X/41/5/057301

Thermoelectrics facilitate the direct conversion of heat and electric power, devoid of any moving parts or liquid media.[1] As the global development model transitions from rapid and aggressive practices to one centered on green, environmentally friendly, and sustainable development. Thermoelectric materials have emerged as a new class of energy conversion materials garnering significant attention from researchers.[2] Thermoelectrics are anticipated to play an important role in energy production and transformation. The dimensionless thermoelectric figure-of-merit ZT is defined as $ZT = \sigma S^2 T/(\kappa_{\rm e} + \kappa_{\rm ph})$, where S is the Seebeck coefficient, σ is the electrical conductivity, and T is absolute temperature.[3,4] Here σS^2 is the power factor (PF), $(\kappa_{\rm e} + \kappa_{\rm ph})$ represents the total thermal conductivity κ, which is the sum of the carrier thermal conductivity $\kappa_{\rm e}$ and the lattice thermal conductivity $\kappa_{\rm ph}$.[5,6] Thus, achieving a higher power factor and lower thermal conductivity is imperative for enhancing the performance of thermoelectric materials. Typically, the electrical properties of materials can be enhanced through strategies such as introducing resonance levels,[7,8] adjusting band structures,[9,10] energy filtering effect,[11] and alloying methods.[12,13] Simultaneously, the independent parameter $\kappa_{\rm ph}$ can be optimized through techniques that enhance phonon scattering, such as striking interstitial effect,[14–16] the defect engineering is like spot defects,[17] and lattice softening effect.[18–20] These approaches prove to be effective methods for enhancing thermoelectric performance.

The spark plasma sintering (SPS) is the widely used technology to sinter thermoelectric compounds.[21] With the advancement of preparation technology and scientific research, an increasing number of innovative fabrication methods are being continuously developed and refined, among which high-pressure technology has been proved as a novel approach in manipulating the properties of materials.[22–24] The approach offers the advantages of rapid synthesis, a straightforward preparation process, and the enhancement of various material properties through tuning the geometry and electronic structures.[25–27] Jia *et al.* revealed that under high pressure (5.2 GPa), the carrier concentration of PbTe is more than ten times of

†These authors contributed equally to this work.
*Corresponding authors. Email: hairuisun1216@qfnu.edu.cn; yshzhang@qfnu.edu.cn; xiaobing.phy@qfnu.edu.cn
© 2024 Chinese Physical Society and IOP Publishing Ltd

that achieved through standard doping methods at normal pressure. Consequently, the high-pressure synthesized PbTe compound exhibits enhanced electrical transport properties. The ZT value of PbTe measured at ambient temperature is 0.87.[28] Furthermore, high-pressure techniques can create intricate morphologies, such as grain boundaries, dislocations, and defects within bulk materials, effectively scattering phonons and suppressing $\kappa_{\rm ph}$,[29] acting important role on the properties of materials.

PbTe is a traditional excellent thermoelectric material, with the maximum ZT value of 2.3.[30] However, it contains the toxic Pb element. As the lead-free sister compound of PbTe, SnTe has been attracted much attention due to the environmentally friendly elements, and the similar crystal and band structures.[31] Nevertheless, SnTe suffers from the seriously low thermoelectric properties (the ZT value of pristine SnTe compound is $\sim$0.21 at 750 K[32]). This is due to (i) the high intrinsic Sn vacancies leading to an exceptionally high hole concentration $\sim 5 \times 10^{20}\,{\rm cm}^{-3}$–$10^{21}\,{\rm cm}^{-3}$,[33,34] (ii) the large valence band offset between the L and Σ positions [$\Delta E(L-\Sigma) = 0.3$–0.4 eV compared to 0.2 eV in PbTe].[35,36] Consequently, SnTe represents notably the low S and remarkably high κ. This unfavorable combination restricts its viability as high-performance thermoelectrics.[37] Zhang *et al.* employed the ball milling method to introduce complex nano-microstructure to reduce κ, achieving a ZT value of $\sim$0.45 at 750 K for the pristine SnTe compound.[38] The enhancement can be attributed to the adjustment of microstructure through ball milling, resulting in an increased grain boundary density to reduce $\kappa_{\rm ph}$. In recent years, the defect engineering has been adopted to optimize the performance of SnTe, such as doping indium (In) in SnTe can introduce the resonance energy levels to enhance the S and to achieve the ZT value of 1.1.[38] Alloying Cd with SnTe induces the convergence of the valence band, leading to an increase in the S and the ZT value of $\sim$0.96 at 873 K.[39] Even so, it exists a big challenge to consider the solubility limit and the precisely controlling the dopant behaviors.[40]

In this work, we employ the simple and fast method to fabricate the pristine SnTe compounds via high-pressure and high-temperature (HPHT) method, and investigate the impact of high pressure on the thermoelectric properties and energy band structure of SnTe. We establish the feasibility of collaboratively optimizing the S and κ through the high-pressure method. With the increase in synthetic pressure (1–5 GPa), the carrier concentration ($n_{\rm H}$) of SnTe can be effectually reduced, decreasing the unexpectedly high $n_{\rm H}$ in the sample. Our theoretical calculations indicate that with an increase in pressure, the energy separation between the light- and heavy-hole valence bands in SnTe decreases, leading to the convergence of energy bands. Combining the relatively low $n_{\rm H}$ with the band convergency effect, the S increases for the high-pressure sintered SnTe compounds. More importantly, high pressure modifies the microstructure of SnTe, introducing a wealth of dislocations and lattice distortions, exerting a substantial influence on the phonon scatterings to reduce κ. The high-pressure method realizes the collaborative optimization of thermal and electrical properties, and the sample sintered at 5 GPa achieves a ZT value of 0.51 at 750 K, which is the top level in pristine SnTe. Our work provides significant insights into the optimization of thermoelectric properties through high pressure.

Experimental. The high-purity tin (99.99%) and tellurium (99.999%) powders were weighed according to atomic ratio 1:1 by a high-precision balance (a scale sensitivity of 0.0001 g). The mixed powders were ground for 30 min at ambient temperature in the glove box with the protection of argon, and then placed into a 10-mm-diameter quartz tube. The vacuum within the tube was reduced to below 10^{-4} Torr before sealing. The sealed quartz tube was then put into the muffle furnace, took two hours to heat to 650 ℃, and was maintained for 40 h. Subsequently, temperature was elevated to 900 ℃ within one hour, held constant for 10 h, and naturally cooled down to room temperature.

The obtained SnTe ingot was ground into powder with the uniform particle size. The powder was assembled into a magnesium oxide cavity with a diameter of 12 mm. The tantalum sheets and hexagonal boron nitride powder were employed as a protective layer to isolate the sample from the cavity, ensuring the purity of sample. Sintering was conducted under different sintering pressures (1, 2, 3, 4, and 5 GPa) using a cubic large volume press (ZN-460, China), supplying a strictly sealed and vacuum environment, which effectively suppresses any volatilization behavior of SnTe samples at high temperatures and ensures the stability of the components. The sintering temperature was set at 1273 K for 30 min, respectively. After the sintering program was completed, rapid cooling technology (in 2 min) was adopted. It resulted in obtaining a cylindrical sample with a diameter of 12 mm and a thickness of 4 mm, intending for the next thermal and electrical performance testing.

X-ray diffraction (XRD) tests were conducted with the Rigaku x-ray diffractometer (Rigaku Smartlab SE, 451B-DE-SI-RYR, Japan) to analyze the sample's crystal structure. Microscopic images were acquired through high resolution transmission electron microscopy (HRTEM, JEOL JEM-2100plus). The thermal diffusion coefficient λ was measured by laser flash technology (Netzsch LFA457, Germany). The cylindrical sample was coated with a thin layer of graphite to reduce the error of laser emissivity measurement. The sample density ρ was determined by the Archimedean drainage method, and the κ was calculated by the formula $\kappa = \lambda\rho C_{\rm p}$, where $C_{\rm p}$ is the heat capacity estimated by the Dulong–Petit law. We prepared a sample by cutting and polishing into a $10\times2\times2\,{\rm mm}^3$ cuboid. The σ and S were measured concurrently using ZEM-3 device (ULVAC Riko Japan) within the temperature range from 300 K to 750 K, with an uncertainty of ±5%. Additionally, the Hall test at room temperature was determined using a Hall apparatus (Lake Shore 8404, USA). The $n_{\rm H}$ and carrier mobility ($\mu_{\rm H}$) were subsequently calculated by $n_{\rm H} = 1/eR_{\rm H}$ and $\mu_{\rm H} = \sigma R_{\rm H}$, respectively, where $R_{\rm H}$ is the Hall coefficient. The Vienna *ab initio* simulation pack-

age (VASP) was utilized for the density-functional theory calculations and the Perdew–Burke–Ernzerhof form of the generalized gradient approximation was employed as the electronic exchange-correlation functional. A plane wave cutoff energy of 400 eV was employed, and the reciprocal space integrations were conducted on an $8 \times 8 \times 1$ Monkhorst–Pack k-point mesh. The spin–orbit coupling was used in the calculations to analyze the electronic structures affected by element Te. The geometry structures were relaxed until the forces on each atom are less than 0.001 meV/Å and the stress tensor is below 0.2 kbar.

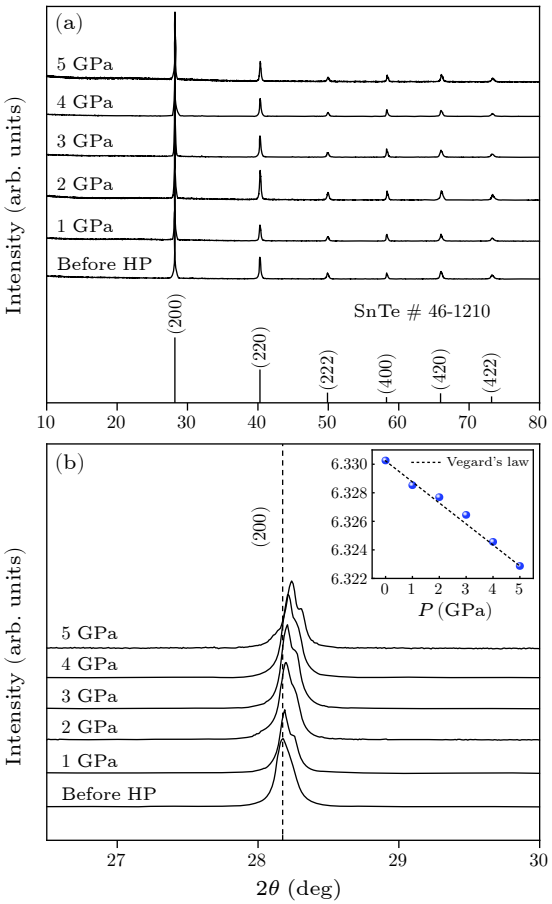

Fig. 1. (a) Powder XRD patterns for samples of sintered under various pressures (1, 2, 3, 4, and 5 GPa) and before HP (high pressure). (b) Zoom-in view of the XRD patterns (2θ ranging between 26.5° and 30°). The illustration is the change of lattice parameters with the sintering pressure rise.

Results and Discussion. SnTe undergoes various structural phase transitions in response to pressure: at room temperature, the phase transition from the low-pressure phase (the space group of $Fm\bar{3}m$) to the high-pressure phase (the space group of $Pnma$) occurs at 4.1 GPa.[41] To investigate the impact of pressure on the crystal structure of SnTe, XRD test was conducted. Figure 1(a) depicts the XRD patterns of SnTe samples sintered under various pressures (1, 2, 3, 4, and 5 GPa) and before HP (high pressure). We can observe that all samples exhibit peaks consistent with the rock salt structure (space group $Fm\bar{3}m$),[42] without observed impurity phases, and the orientation of XRD patterns does not change before and after sintering. This indicates the reversibility of the structural phase transition in SnTe induced by pressure, with the sample returning to the $Fm\bar{3}m$ space group when restored to normal pressure. The main peaks ($2\theta \approx 28.3°$) of the samples slightly shift to high angle with the sintered pressure increasing, as shown in Fig. 1(b). Drawing upon the XRD data illustrated in Fig. 1(a), we have computed the lattice constants for our samples subjected to varying sintering pressures, as shown in the inset of Fig. 1(b). It is noteworthy that these calculated constants demonstrate a decreasing trend with an increase in the applied sintering pressure, exhibiting lower values compared to that of the SPS-sintered samples,[43,44] which is consistent with the observed shift in the XRD patterns. The decrease in lattice spacing suggests a gradual reduction in the volume of the SnTe cell as pressure increases.

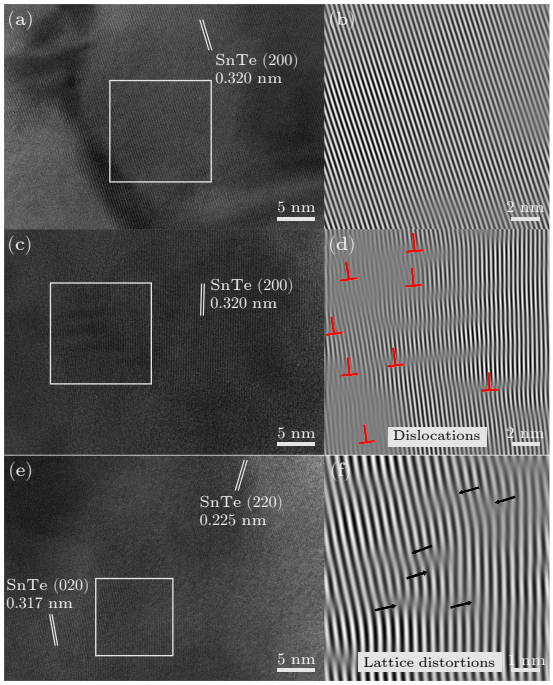

Fig. 2. (a) HRTEM image of SnTe sample sintered at 1 GPa. (b) The inverse Fourier transform (IFFT) images of square area in (a). [(c), (e)] HRTEM images of different regions in the SnTe sample sintered at 5 GPa. [(d), (f)] The IFFT images of square areas in (c) and (e), respectively.

To examine the micro-morphology of SnTe samples sintered under high pressure, we present the HRTEM studies of sample sintered at different pressures. As we can see in Fig. 2(a), SnTe sintered at low pressure (1 GPa) included a large range of neatly arranged planes, which are characterized by a well-defined spacing of 0.320 nm, and they were identified as the (200) crystal plane of SnTe. From the IFFT image [Fig. 2(b)], no dislocations can be observed within the SnTe matrix. With increasing the sintered pressure to 5 GPa, in addition to the (200) plane [Fig. 2(c)], we also observed the (020) and (220) planes [Fig. 2(e)] in our sample, which are characterized by the spacings of 0.317 nm and 0.225 nm, respectively. Unlike the SnTe

compound sintered at 1 GPa, a large number of dislocations can be found after the high-pressure (5 GPa) sintering [Fig. 2(d)]. In addition, as shown in in Fig. 2(f), the distinct lattice distortions are observed as well. The high density dislocations and lattice distortions are due to the high-pressure effect: The microstructure of SnTe nanoparticles undergoes the lattice constants shrinkage and phase transition with the increasing pressure to 5 GPa. After the pressure release, the lattice constants and even the high-pressure phase try to recover back to the low-pressure phase and the corresponding lattice constants. During the recovery process, lattice planes exert mutual compression upon each other, thereby introducing a large number of lattice defects in our sample, such as dislocations and distortions, among others. The micro-morphology modification by high-pressure brought will enhance the phonon scatterings to reduce $\kappa_{\rm ph}$.

Table 1. Measured Hall coefficient $R_{\rm H}$, Hall carrier concentration $n_{\rm H}$ and Hall mobility $\mu_{\rm H}$ of SnTe samples at room temperature.

Sintering pressure (GPa)	Hall coefficient $R_{\rm H}$ ($\rm cm^3{\cdot}C^{-1}$)	Carrier concentration $n_{\rm H}$ (10^{20} $\rm cm^{-3}$)	Hall mobility $\mu_{\rm H}$ ($\rm cm^2{\cdot}V^{-1}{\cdot}s^{-1}$)
1	0.021	2.92	147.5
2	0.037	1.85	215.8
3	0.046	1.35	328.5
4	0.047	1.32	349.8
5	0.059	1.06	372.3

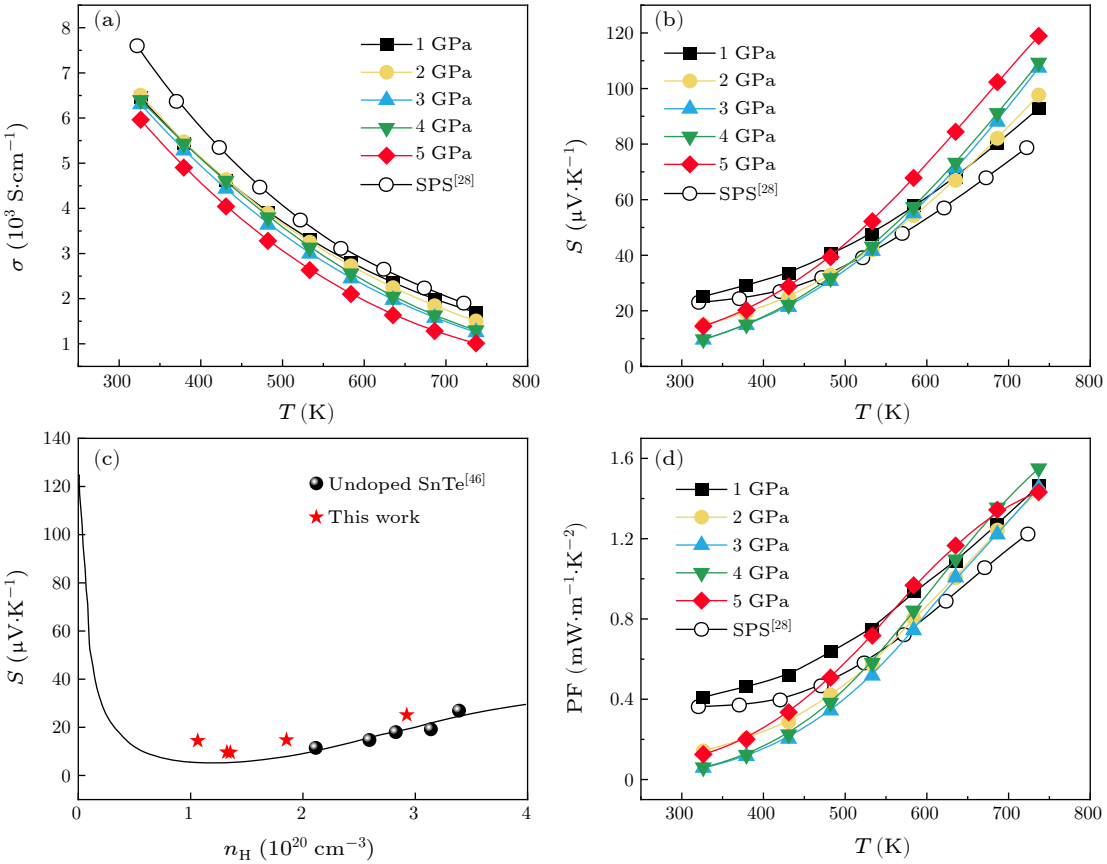

Fig. 3. Temperature-dependent change of (a) electrical conductivity σ and (b) Seebeck coefficient S. (c) S at room temperature versus $n_{\rm H}$. The solid line represents the Pisarenko curve. (d) Temperature-dependent change of power factor.

To understand the impact of high pressure on the electrical transport properties, we firstly conducted the Hall tests on all these pristine SnTe samples at room temperature, as summarized in Table 1. The positive Hall coefficients indicate that these samples exhibit the P-type conductivity. It is well-known that the pristine SnTe compound presents a relatively high carrier concentration ($\sim 5\times10^{20}$ $\rm cm^{-3}$–10^{21} $\rm cm^{-3}$ [33,34]), due to a large amount of Sn vacancies.[45] Interestingly, with increasing pressure, the $n_{\rm H}$ decreases from 2.92×10^{20} $\rm cm^{-3}$ (sintered at 1 GPa) to 1.06×10^{20} $\rm cm^{-3}$ (sintered at 5 GPa), which is lower than that of the SPS sample. The decreasing $n_{\rm H}$ reflects that pressure can partly suppress the formation of Sn vacancies or facilitate Sn atoms filling their own vacancies. This is due to the decreasing vacancy volume (which is consistent with the XRD results), leading to an increase in repulsive interatomic interactions, further leading to the increase in vacancy formation energy with increasing pressure.[46,47] On the other hand, for $\mu_{\rm H}$, the SnTe sample sintered by SPS has a low value ($\sim 100\,\rm cm^2{\cdot}V^{-1}{\cdot}s^{-1}$ [48]), which is due to its high Sn vacancy concentration inducing the strong carrier scatterings. For our sample sintered at 1 GPa, the

μ_H increases to 147.5 $cm^2 \cdot V^{-1} \cdot s^{-1}$, which is of profits from the reduced Sn vacancy concentrations. As the sintering pressure increases up to 5 GPa, the μ_H further increases to 372.3 $cm^2 \cdot V^{-1} \cdot s^{-1}$. This result is highly beneficial for optimizing electrical properties.

We then conducted the measurements of temperature dependence of S, σ, and PF, as shown in Fig. 3. It is obvious that σ decreases with the increasing temperature, while S tends to reverse, exhibiting typical degenerate semiconducting behavior. Compared with the σ of the sample synthesized by SPS (7.6×10^3 S·cm^{-1}),[32] the sample sintered at 5 GPa demonstrates a decreased value of 5.96×10^3 S·cm^{-1}. The high-pressure sintered compounds all have comparatively low σ, which is due to the significantly decreased n_H. With increasing pressure from 1 GPa to 5 GPa, although the μ_H gradually increases, it cannot catch up with the speed of n_H decreasing. Therefore, the σ of the SnTe compounds decrease with pressure. For the S, SnTe compounds sintered under high pressure possess higher S than the SPS sintered compounds, especially in the high-temperature region. With sintering pressure increasing, the S increases to 118.9 μV·K^{-1} at 5 GPa and 750 K. Additionally, according to the relationship between n_H and S at room temperature, we plot the Pisarenko curve using the two-valence band model in Fig. 3(c).[49] We notice that the data points of pristine SnTe using SPS (the black circles) are right on the curve.[50] However, for the samples sintered by high pressure, the S (the red stars) can surpass the Pisarenko curve, usually owing to the band convergence. Thus, it is observed in Fig. 3(d) that the PF value of ∼1.5 mW·m^{-1}·K^{-2} was obtained at 750 K, which is slightly higher than those of the (SPS) processed samples.

To clearly understand the pressure effect on the S, we turned to the electronic band structures under pressure, especially for its impact on the band gap and band energy difference $\Delta E(L-\Sigma)$. The band structures of SnTe were calculated, and we noticed that as pressure increases from 0 to 5 GPa as exhibited in Figs. 4(a) and 4(b), the band gap E_g increases from 0.10 eV to 0.25 eV and the energy difference ΔE decreases from 0.250 eV to 0.042 eV. In principle, the decreasing $\Delta E(L-\Sigma)$ will facilitate the band convergency and increase the density of state effective mass m_d^*.[51] Based on the Mahan–Sofo theory, the S can be expressed using a simple form formula

$$S = \frac{8\pi^2 k_B^2 T}{3qh^2} m_d^* \left(\frac{\pi}{3n_H}\right)^{2/3}, \tag{1}$$

where k_B is Boltzmann's constant, h is Planck's constant, n_H is the carrier concentration.[52] Therefore, the increased m_d^* (due to the band convergency) and decreased n_H under pressure will boost the S of SnTe compounds. This is consistent well with the experimental results.

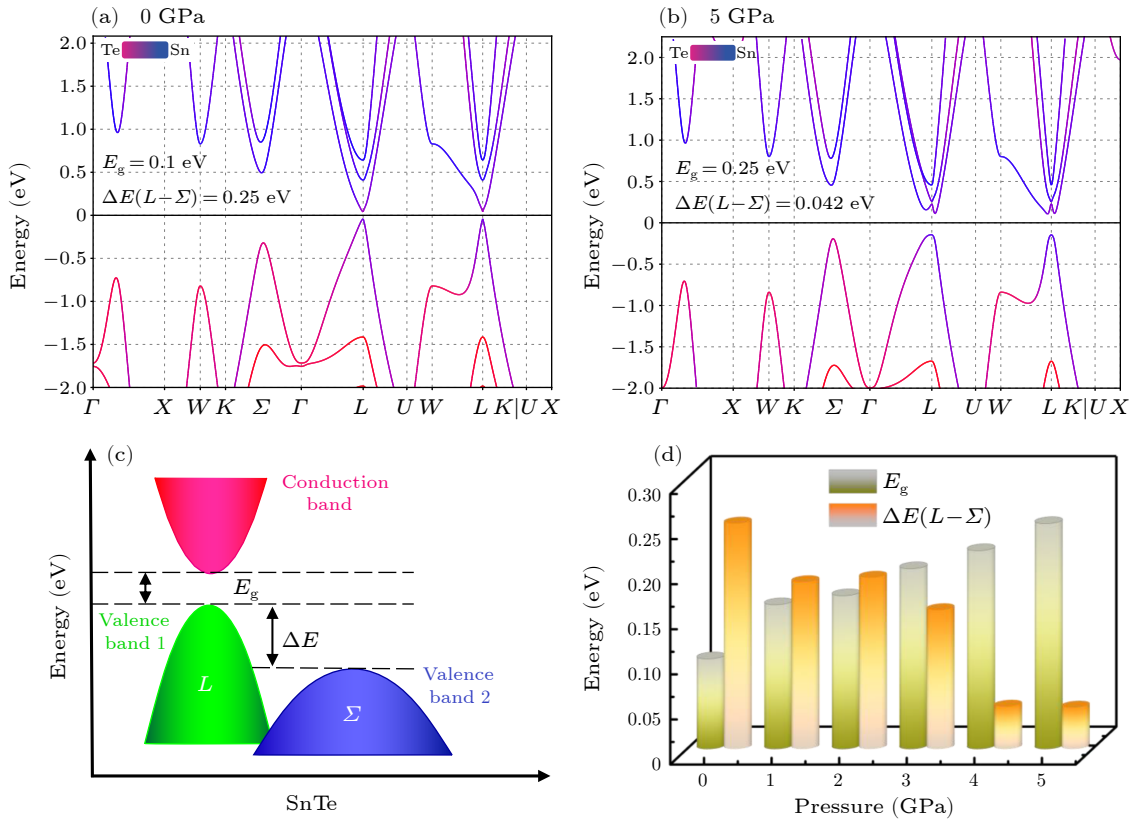

Fig. 4. Electronic band structures of SnTe at (a) 0 GPa and (b) 5 GPa. (c) Schematic view of the band offset between L and Σ positions. (d) The band gaps E_g and energy differences. $\Delta E(L-\Sigma)$ at diverse pressure.

We have known from Fig. 2 that pressure significantly influences the microstructures of SnTe, which will affect the phonon transport conductively. Figure 5 illustrates the thermotransport performance of the sintered samples under various pressures as a function of temperature. In Fig. 5(a), we can observe that with the increase of pressure, the κ of samples sintered under high pressure exhibits a significant decrease, from 7.75 $W{\cdot}m^{-1}{\cdot}K^{-1}$ (sintered at 1 GPa) to 5.47 $W{\cdot}m^{-1}{\cdot}K^{-1}$ (sintered at 5 GPa) at 325 K, reduced by about 30%, which are lower than that using the SPS-sintered SnTe compound.[32] With increasing temperature to 750 K, the κ of the sample sintered at 5 GPa can be lowered to 2.0 $W{\cdot}m^{-1}{\cdot}K^{-1}$. Since the κ includes the carrier and lattice contributions, we separated them by performing calculations of the κ_e and κ_{ph} in accordance with Wedemann–Franz's law $\kappa_e = L\sigma T$, where L represents the Lorentz constant and T is absolute temperature.[53,54] Observably, the κ_e [Fig. 5(b)] experiences a significant decrease attributed to the decrease in σ. Subtracting the κ_e from the total thermal conductivity, we obtained the κ_{ph}. The κ_{ph} of the sample sintered at 5 GPa is even lower than 1.0 $W{\cdot}m^{-1}{\cdot}K^{-1}$, and has the lowest value of $\sim$0.68 $W{\cdot}m^{-1}{\cdot}K^{-1}$. The lower κ_{ph} values are due to the high-pressure induced dislocations and lattice distortions in the SnTe matrix. These defects strongly scatter phonons and depress the κ_{ph} effectively, as shown in Fig. 5(c). To compare the κ with pressure manipulations with those under the doping at 750 K,[55–58] we created a bar chart in Fig. 5(d). It can be seen that the κ_{ph} of our high-pressure sintered SnTe compound is even much lower than those using dopants (Mn, In, and Gd), and comparable with those using the Ca and AgCuTe dopants. This means that only through the high-pressure manipulations, the κ_{ph} can approach to its theoretical limit (0.4 $W{\cdot}m^{-1}{\cdot}K^{-1}$ [57]). However, since dopants are usually to compensate the high hole concentration in the pristine SnTe compound and additionally decrease the n_H,[55] they will present even lower σ than the high-pressure sintered compounds. The value of κ_e for samples sintered under high pressure is relatively high, whereas the corresponding values κ_{ph} belongs to a smaller scale. Therefore, the total thermal conductivity of our pressure-sintered SnTe compounds is even comparable to those using doping, and much lower than those of the previously SPS-sintered compounds. All in all, adjusting the microstructure through high pressure is an efficient method for optimizing the thermal performance.

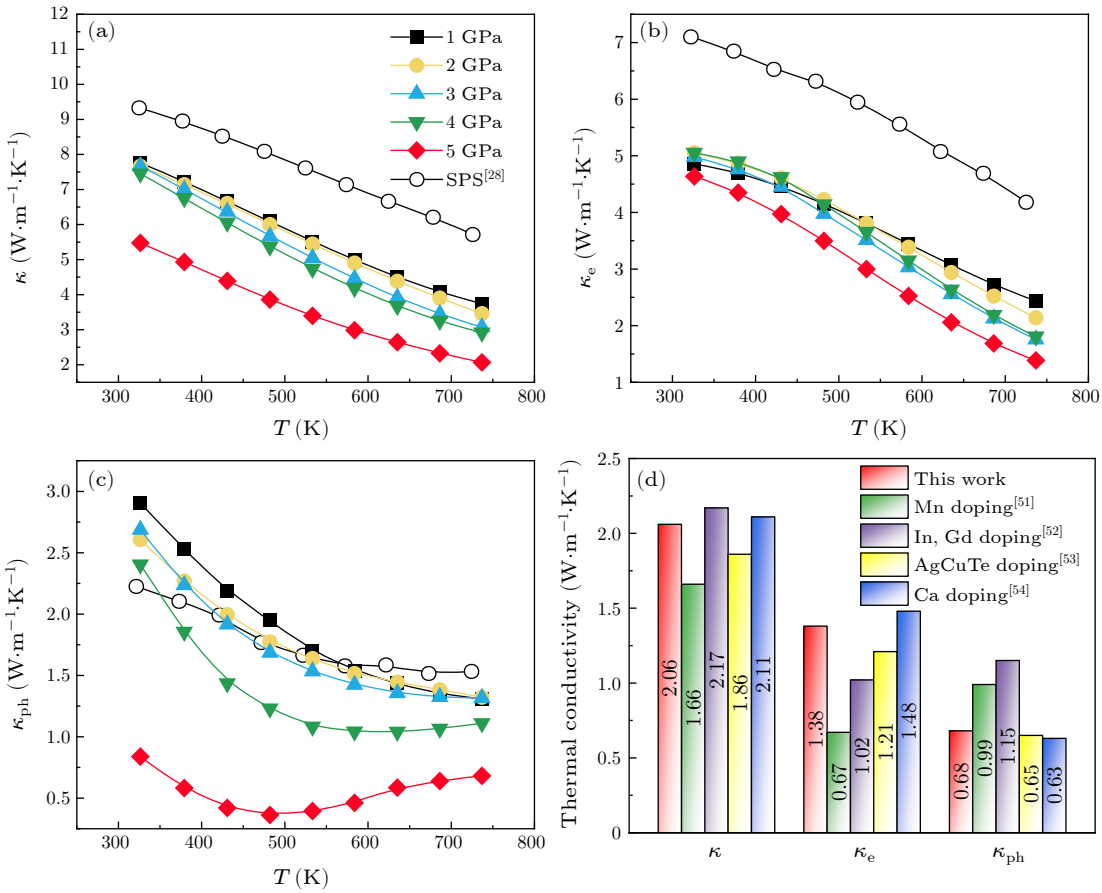

Fig. 5. Thermal transport properties of SnTe samples using different sintered methodologies: (a) total thermal conductivity κ, (b) electric thermal conductivities κ_e, (c) lattice thermal conductivity κ_{ph}, (d) comparison with other works taken from Refs. [55–58].

Based on the electrical and thermal properties, we calculated the ZT values of these SnTe samples sintered at high pressure, as shown in Fig. 6. Obviously, in high temperature section of the test temperature zone, the ZT values of our samples are higher than those using SPS.[32] Additionally, the peak ZT value in our samples increases

from 0.28 (sintered at 1 GPa, 750 K) to 0.51 (sintered at 5 GPa, 750 K), showing a 80% improvement. Compared with the SPS pristine SnTe sample ($\sim$0.21), the maximum ZT value of the sample sintered at 5 GPa is increased by 140%. The largely increased ZT value of pristine SnTe is mainly attributed to the significant reduction in κ. Although the ZT values of these SnTe compounds sintered under high pressure cannot be comparable to those using the defect engineering, such as Ag doped SnTe ($ZT = 1.8$ at 873 K),[40] our work on the pristine SnTe compounds indicates that the high-pressure methodology is highly effective to improve the thermoelectric properties via manipulating the microstructure and band structures. Based on the good pristine SnTe candidates, further defect engineering can be applied to achieve more excellent thermoelectric performance.

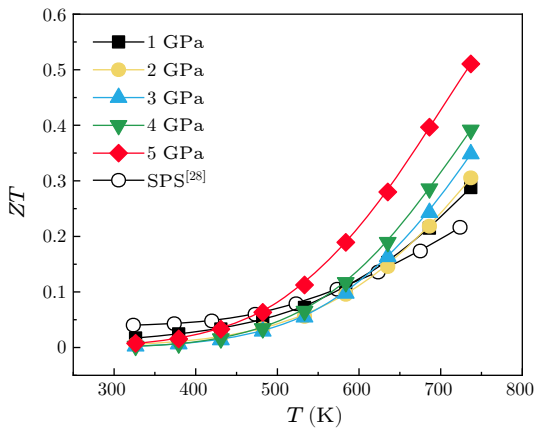

Fig. 6. ZT values as a function of temperature for SnTe sintered at different pressures.

In a word, applying high pressure to sinter the pristine SnTe compounds, we can dramatically manipulate the microstructures and band structures. The pressure induces high density dislocations and lattice distortions in the SnTe matrix offering more phonon scattering centers, leading to a significant reduction in the lattice thermal conductivity to 0.68 $\mathrm{W{\cdot}m^{-1}{\cdot}K^{-1}}$ at 750 K. The total thermal conductivity can be lowered to 2.0 $\mathrm{W{\cdot}m^{-1}{\cdot}K^{-1}}$ at 750 K, which is much lower than that of the SPS-sintered samples. Due to the pressure-suppressed Sn vacancy formation, the hole carrier concentration decreases to 1.06×10^{20} $\mathrm{cm^{-3}}$ in the pristine SnTe compound. Additionally, pressure can facilitate the valence band convergence, thereby enhancing the Seebeck coefficient. The enhancement of the Seebeck coefficient ensures the stability of power factor even when the electrical conductivity is compromised. The significant reduction in thermal conductivity, combined with the steadiness of electrical performance, ultimately results in the ZT value of 0.51 for the sample sintered at 5 GPa, increasing 140% compared to the traditional SPS sintered sample. It is demonstrated that regulating the thermoelectric properties of SnTe material through high pressure holds great potential and prospects, and it provides reference and guidance for other thermoelectric materials.

Acknowledgement. This work was supported by the National Natural Science Foundation of China (Grant Nos. 12374012, 11974208, 52172212, and 52002217) and Shandong Provincial Natural Science Foundation (Grant Nos. ZR2023JQ001, ZR2020YQ05, and 2019KJJ020). Y. Zhang acknowledges financial support from the Program of Distinguished Expert of Taishan Scholar (Grant No. tstp20221124).

References

[1] Li W, Xu T, Ma Z, Haruna A Y, Jiang Q H, Luo Y B, and Yang J Y 2021 *Chin. Phys. Lett.* **38** 097201
[2] Chen T, Qin X Y, Ming H W, Zhang X M, Wang Z Y, Yang S H, Zhang Y S, Ge Z H, Xin H X, Li D, and Zhang J 2023 *Chem. Eng. J.* **467** 143397
[3] Liu Z T, Hong T, Xu L Q, Wang S N, Gao X, Chang C, Ding X D, Xiao Y, and Zhao L D 2023 *Interdiscip. Mater.* **2** 161
[4] Zhu K, Deng B, Qian X, Wang Y, Li H, Jiang P, Yang R, and Liu W 2022 *InfoMat* **4** e12324 (in Chinese)
[5] Tang X, Li Z, Liu W, Zhang Q, and Uher C 2022 *Interdiscip. Mater.* **1** 88
[6] Wang T Y, Duan X L, Zhang H, Ma J L, Zhu H T, Qian X, Yang J Y, Liu T H, and Yang R G 2023 *InfoMat* **5** e12481 (in Chinese)
[7] Yang Q, Lyu T, Li Z, Mi H, Dong Y, Zheng H, Sun Z, Feng W, and Xu G 2021 *J. Alloys Compd.* **852** 156989
[8] Hussain T, Li X T, Danish M H, Rehman M U, Zhang J, Li D, Chen G, and Tang G D 2020 *Nano Energy* **73** 104832
[9] Tan G, Hao S, Cai S, Bailey T P, Luo Z, Hadar I, Uher C, Dravid V P, Wolverton C, and Kanatzidis M G 2019 *J. Am. Chem. Soc.* **141** 4480
[10] Pei Y, Wang H, and Snyder G J 2012 *Adv. Mater.* **24** 6125
[11] Shakouri A, LaBounty C, Abraham P, Piprek J, and Bowers J E 1999 *Mater. Res. Soc. Proc.* **545** 449
[12] Li J, Zhang X Y, Lin S Q, Chen Z W, and Pei Y Z 2017 *Chem. Mater.* **29** 605
[13] Fu T Z, Xin J Z, Zhu T J, Shen J J, Fang T, and Zhao X B 2019 *Sci. Bull.* **64** 1024
[14] Liu Z, Sato N, Gao W, Yubuta K, Kawamoto N, Mitome M, Kurashima K, Owada Y, Nagase K, Lee C, Yi J, Tsuchiya K, and Mori T 2021 *Joule* **5** 1196
[15] Biswas K, He J, Blum I D, Wu C I, Hogan T P, Seidman D N, Dravid V P, and Kanatzidis M G 2012 *Nature* **489** 414
[16] Poudel B, Hao Q, Ma Y *et al.* 2008 *Science* **320** 634
[17] Fu L, Yin M, Wu D, Li W, Feng D, Huang L, and He J 2017 *Energy Environ. Sci.* **10** 2030
[18] Zhao L D, Lo S H, Zhang Y S, Sun H, Tan G J, Uher C, Wolverton C, Dravid V P, and Kanatzidis M G 2014 *Nature* **508** 373
[19] Morelli D T, Jovovic V, and Heremans J P 2008 *Phys. Rev. Lett.* **101** 035901
[20] Muchtar A, Srinivasan B, Tonquesse S, Singh S, Soelami N, Yuliarto B, Berthebaud D, and Mori T 2021 *Adv. Energy Mater.* **11** 2101122
[21] Yang D, Yao W, Yan Y, Qiu W, Guo L, Lu X, Uher C, Han X, Wang G, Yang T, and Zhou X 2017 *NPG Asia Mater.* **9** e387
[22] Li Y, Sun S, He Y, and Li H 2022 *Chin. Phys. Lett.* **39** 026101
[23] Fan C, Liu S, Liu J, Wu B, Tang Q, Tao Y, Pu M, Zhang F, Li J, Wang X, He D, Zhou C, and Lei L 2022 *Chin. Phys. Lett.* **39** 026401

[24] He X, Zhang C L, Li Z W, Zhang S J, Min B S, Zhang J, Lu K, Zhao J F, Shi L C, Peng Y, Wang X C, Feng S M, Song J, Wang L H, Prakapenka V B, Chariton S, Liu H Z, and Jin C Q 2023 *Chin. Phys. Lett.* **40** 057404

[25] Zhang Y, Hao X, Huang Y, Tian F, Li D, Wang Y, Song H, and Duan D 2021 *Chin. Phys. Lett.* **38** 026101

[26] Liu C, Wang J, Deng X, Wang X, Pickard C J, Helled R, Wu Z, Wang H T, Xing D, and Sun J 2022 *Chin. Phys. Lett.* **39** 076101

[27] Wang Y, Yao M, Hua X, Jin F, Yao Z, Yang H, Liu Z, Li Q, Liu R, Liu B, Jiang L, and Liu B 2022 *Chin. Phys. Lett.* **39** 056101

[28] Zhu P W, Jia X, Chen H Y, Chen L X, Guo W L, Mei D L, Liu B B, Ma H A, Ren G Z, and Zou G T 2002 *Chem. Phys. Lett.* **359** 89

[29] Yang M, Sun H, Zhou X, Chen X, Su T, and Liu X 2022 *J. Alloys Compd.* **910** 164827

[30] Wu D, Zhao L D, Tong X, Li W, Wu L J, Tan Q, Pei Y L, Huang L, Li J F, Zhu Y M, Kanatzidis M G, and He J Q 2015 *Energy Environ. Sci.* **8** 2056

[31] Banik A and Biswas K 2014 *J. Mater. Chem. A* **2** 9620

[32] Zhang X M, Wang Z Y, Zou B, Brod M K, Zhu J B, Jia T T, Tang G D, Snyder G J, and Zhang Y S 2021 *Chem. Mater.* **33** 9624

[33] He J, Tan X J, Xu J T, Liu G Q, Shao H Z, Fu Y J, Wang X, Liu Z, Xu J Q, Jiang H C, and Jiang J 2015 *J. Mater. Chem. A* **3** 19974

[34] Ortiz B R, Adamczyk J M, Gordiz K, Braden T, and Toberer E S 2019 *Mol. Syst. Des. Eng.* **4** 407

[35] Rogers L M 1968 *J. Phys. D. Appl. Phys.* **1** 1067

[36] Zhao L D, Wu H J, Hao S Q, Wu C I, Zhou X Y, Biswas K, He J Q, Hogan T P, Uher C, Wolverton C, Dravid V P, and Kanatzidis M G 2013 *Energy Environ. Sci.* **6** 3346

[37] Li W, Zheng L, Ge B, Lin S, Zhang X, Chen Z, Chang Y, and Pei Y 2017 *Adv. Mater.* **29** 1605887

[38] Zhang Q, Liao B, Lan Y, Lukas K, Liu W, Esfarjani K, Opeil C, Broido D, Chen G, and Ren Z 2013 *Proc. Natl. Acad. Sci. USA* **110** 13261

[39] Tan G J, Zhao L D, Shi F Y, Doak J W, Lo S H, Sun H, Wolverton C, Dravid V P, Uher C, and Kanatzidis M G 2014 *J. Am. Chem. Soc.* **136** 7006

[40] Liu Y, Zhang X, Nan P, Zou B, Zhang Q, Hou Y, Li S, Gong Y, Liu Q, Ge B, Cojocaru-Mirédin O, Yu Y, Zhang Y, Chen G, Wuttig M, and Tang G 2022 *Adv. Funct. Mater.* **32** 2209980

[41] Zhou D, Li Q, Ma Y, Cui Q, and Chen C 2013 *J. Phys. Chem. C* **117** 5352

[42] Zhou D, Li Q, Ma Y, Cui Q, and Chen C 2013 *J. Phys. Chem. C* **117** 8437

[43] Guo F, Zhu J, Cui B, Sun Y, Zhang X, Cai W, and Sui J 2022 *Acta Mater.* **231** 117922

[44] Aminzare M, Tseng Y C, Ramakrishnan A, Chen K H, and Mozharivskyj Y 2019 *Sustainable Energy Fuels* **3** 251

[45] Tan X, Tan X, Liu G, Xu J, Shao H, Hu H, Jin M, Jiang H, and Jiang J 2017 *J. Mater. Chem. C* **5** 7504

[46] Mukherjee S, Cohen R E, and Gülseren O 2003 *J. Phys.: Condens. Mater.* **15** 855

[47] Ouyang G, Zhu W G, Yang G W, and Zhu Z M 2010 *J. Phys. Chem. C* **114** 4929

[48] Pei Y, Zheng L, Li W, Lin S, Chen Z, Wang Y, Xu X, Yu H, Chen Y, and Ge B 2016 *Adv. Electron. Mater.* **2** 1600019

[49] Ioffe A F, Stil'bans L S, Iordanishvili E K, Stavitskaya T S, Gelbtuch A, and Vineyard G 1959 *Phys. Today* **12** 42

[50] Brebrick R F and Strauss A J 1963 *Phys. Rev.* **131** 104

[51] Pei Y Z, LaLonde A, Iwanaga S, and Snyder G J 2011 *Energy Environ. Sci.* **4** 2085

[52] Tan G J, Shi F Y, Doak J W, Sun H, Zhao L D, Wang P L, Uher C, Wolverton C, Dravid V P, and Kanatzidis M G 2015 *Energy Environ. Sci.* **8** 267

[53] Kim H S, Gibbs Z M, Tang Y, Wang H, and Snyder G J 2015 *APL Mater.* **3** 041506

[54] Zhu H, Li Z, Zhao C X, Li X X, Yang J L, Xiao C, and Xie Y 2021 *Natl. Sci. Rev.* **8** nwaa085

[55] Tan G J, Shi F Y, Hao S Q, Chi H, Bailey T P, Zhao L D, Uher C, Wolverton C, Dravid V P, and Kanatzidis M G 2015 *J. Am. Chem. Soc.* **137** 11507

[56] Tan G, Shi F, Hao S, Chi H, Zhao L D, Uher C, Wolverton C, Dravid V P, and Kanatzidis M G 2015 *J. Am. Chem.* **137** 5100

[57] Wu G, Guo Z, Tan X J, Wang R Y, Zhang Q, Hu H Y, Sun P, Wu J H, Liu G Q, and Jiang J 2023 *J. Mater. Chem. A* **11** 649

[58] Al Rahal Al Orabi R, Mecholsky N A, Hwang J, Kim W, Rhyee J S, Wee D, and Fornari M 2016 *Chem. Mater.* **28** 376